International Society for Biofabrication
PURPOSE-LED PUBLISHING™

PAPER • **OPEN ACCESS**

An automated pipeline for tracking and measuring cell spheroids encapsulated in 3D hydrogel systems

To cite this article: Monize Caiado Decarli *et al* 2026 *Biofabrication* **18** 025009

Biofabrication

OPEN ACCESS

RECEIVED
12 September 2025

REVISED
26 January 2026

ACCEPTED FOR PUBLICATION
20 February 2026

PUBLISHED
12 March 2026

PAPER

An automated pipeline for tracking and measuring cell spheroids encapsulated in 3D hydrogel systems

Monize Caiado Decarli[1,2,3,5,*], **Adrián Seijas-Gamardo**[1,5], **Timo Rademakers**[1], **Ane Albillos Sanchez**[1], **Paul Wieringa**[1], **Jorge Vicente L Silva**[4,†], **Ângela Maria Moraes**[2], **Lorenzo Moroni**[1] and **Carlos Mota**[1,*]

[1] MERLN Institute for Technology-Inspired Regenerative Medicine, Department of Complex Tissue Regeneration, Maastricht University, Universiteitssingel, 40, Maastricht, The Netherlands
[2] School of Chemical Engineering, University of Campinas-UNICAMP, Av. Albert Einstein, 500; 13083-852, Cidade Universitária 'Zeferino Vaz', Campinas, SP, Brazil
[3] Department of Biomaterials & Biomedical Technology, University Medical Center Groningen/ University of Groningen, A. Deusinglaan 1, AV 9713 Groningen, The Netherlands
[4] Three-Dimensional Technologies Research Group, CTI Renato Archer, Rodovia Dom Pedro I SP-65, Km 143, 6, 13069-901 Amarais—Campinas, SP, Brazil
[5] The authors contributed equally to this work.
[†] Unfortunately, recently passed away.
[*] Authors to whom any correspondence should be addressed.

E-mail: m.caiado.decarli@umcg.nl and c.mota@maastrichtuniversity.nl

Keywords: spheroid, hydrogel, cellular dynamics, microscopy, automated tracking analysis

Supplementary material for this article is available online

Abstract

Cell spheroids have been exploited as fundamental engineering units applied as screening platforms or assembled as building blocks for tissue engineering applications. While spheroid encapsulation into hydrogels creates more reliable 3D models, it also brings several constraints, e.g., hydrogel swelling and dynamicity, shading, limitations on depth-resolution, and cell staining strategies for monitoring long real-time imaging. Hence, the objective of this work was to develop a post-imaging automated pipeline for the accurate tracking and measuring of spheroids encapsulated in 3D hydrogels. Using NIS Elements ARv5.30 (Nikon) software, we created a sequence of functions for enhancing spheroid borders, extending the depth of focus, reducing hydrogel shading, and identifying coordinates in an automated manner for time-lapse microscopy analysis up to 70 h. Additionally, we established a method for identifying and tracking migration trajectories of protruded cell clusters that detached from spheroids into the hydrogel. For a comparative hydrogel analysis, fluorescent beads were encapsulated in the ionically crosslinked xanthan gum–alginate (XG–Alg) and photocrosslinked methacrylate hyaluronic acid (HAMA). For pipeline validation, human mesenchymal stem cell spheroids were encapsulated in XG–Alg hydrogel. By employing our pipeline, a high dynamicity and intense swelling effect were detected within XG–Alg, while HAMA remained stable, without noticeable movements up to 60 h. Accurate imaging and tracking detected several spheroid morphological changes, including reversible spheroid-ellipsoid shapes, axis rotational motion, outermost layer movements, spheroid fusion, and a spheroid migration speed of approximately 1.3 μm h^{-1}. Protruded cell clusters were detected in high numbers (83–173 per spheroid), migrating arbitrarily into the hydrogel (16°–311°), with an average speed of approximately 11.4 μm h^{-1}. Our results indicate that this automated pipeline can facilitate the understanding of several cellular dynamic events with high accuracy and low manual interference, which are essential for scaling up tissue engineering and other advanced applications such as drug screening platforms.

1. Introduction

Cell aggregates have been exploited as fundamental bioengineering units and can be used as 3D screening platforms or assembled as building blocks for tissue replacement in regenerative medicine [1–3]. Cell aggregates can be arranged into a variety of densely packed 3D configurations, with the spheroid being the simplest and widely used [2], and the organoid representing a more advanced 3D model with significantly increased complexity [4]. Cell aggregate formation typically begins with cell clustering, followed by compaction, which is mainly driven by strong cell–cell interactions and adhesion to secreted extracellular matrix (ECM) components. Once formed, densely packed cells secrete ECM and continuously reorganize and remodel their endogenous microenvironment in response to environmental and physiological conditions [2].

Due to their 3D structure, spheroids exhibit internal gradients of nutrients and cell waste, and the ECM density during compaction and remodeling determines the diffusion rates, consequently impacting metabolic pathways and cell viability [2, 5]. Since compactness and remodeling are dependent on spheroid size, assessing shape parameters in real-time is valuable for determining their viability and functionality, as well as for correlating with biological processes such as differentiation, migration, and fusion of human mesenchymal stromal cells (hMSCs) for tissue engineering applications [6–10]. Indeed, hMSCs spheroids have shown intense compactness and shape retraction during prolonged culture in basal media, with a substantial impact on their cell differentiation potential [11]. Spheroids are also reshaping pre-clinical drug development by providing more accurate assessments for drug efficacy and toxicity trials. For these *in vitro* assays, regular and well-rounded spheroids are more stable and have shown less variability [12]. Therefore, monitoring shape parameters (e.g., diameter, sphericity, area, perimeter, and Feret diameter) over time is essential for controlling variability and improving the reproducibility of spheroids, thereby ensuring the efficacy of toxicity trials.

Spheroids and, more recently, organoids, have been encapsulated in hydrophilic hydrogels to create physiologically relevant 3D *in vitro* models for tissue engineering or drug screening applications. Examples comprise blends of xanthan gum (XG) and alginate (Alg) [13] or alginate-hyaluronic acid [14], and methacrylate hyaluronic acid [15] or gelatin [16]. Hydrogels have viscoelastic properties that provide a favorable biomimetic environment similar to the natural ECM, known to enhance cell proliferation and differentiation [17, 18]. Hydrogels can also offer mechanical support to sustain spheroid fusion over long culturing periods. Hence, hydrogels are frequently used in combination with spheroids or organoids in automated deposition processes such as bioprinting [8, 13–16]. However, due to their larger structure, 3D models exhibit a massive resistance to movement or fusion with neighboring 3D aggregates when embedded in a hydrogel network compared to a liquid culture medium. Solute diffusion in hydrogels is also delayed due to mass transfer hindrance effects [13, 19]. Thus, finding the ideal hydrogel viscosity that provides adequate mechanical support while allowing cell aggregate migration and ensuring the availability of nutrients remains a challenging task.

Inside hydrogels, cells located in spheroids communicate with neighboring spheroids through paracrine mechanisms, secreting signaling molecules that enable long-distance cell–cell communication (e.g. extracellular vesicles, mRNA, and miRNAs [20, 21]). Communication can also occur through physical contact between cell sprouting or protruding mechanisms [22, 23]. However, both chemical and physical communication mechanisms are affected by the spheroid–spheroid distance and the resistance of the hydrogel matrix to mass transfer [2]. It has been reported that 250 μm is the maximum distance for effective diffusion of paracrine signaling molecules capable of acting on ECM homeostasis, angiogenesis, migration, and cell proliferation [22, 24, 25]. However, this distance is affected by the type and composition of the hydrogel employed, and its influence is often underestimated [26].

It is clear that the more viscous the matrix, the more challenging spheroid migration will be. However, the impact caused by the type of polymeric network is crucial. While linear and fibrillar chain hydrogels (e.g. collagen [27] or Alg [28]) tend to offer a structural role that may facilitate migration, branched and high molecular weight hydrogels (e.g. polysaccharides-based) can easily entrap spheroids within their network, impairing any kind of movement. Nonetheless, in the previous study by Decarli *et al* [13] it was demonstrated that XG–Alg blends were successfully employed to encapsulate hMSC spheroids for bioprinting and cell differentiation into larger cartilaginous constructs [13]. Likewise, in the previous study by Sanchez *et al* [15] it was demonstrated that successful migration, fusion, and differentiation of spheroids within hyaluronic acid methacrylate (HAMA). This indicates that the polymeric structure, the degree of modification, and crosslinking critically influence spheroid motility and interaction [15, 29].

Other strategies to modulate spheroid migration kinetics within hydrogels have also been explored, primarily based on the incorporation of structural guidance cues via aligned patterns within hydrogels

or chemical functionalization incorporating cell-binding molecules. Some examples are the use of a collagen matrix aligned with a magnetic field-induced flow [27], functionalization with tagged recombinant N-cadherins [30], or hydrogel functionalization with the RGD peptides, the most widely used approach for enhancing the migration of cells and spheroids [28].

Monitoring cell spheroids encapsulated in hydrogels in real-time is not trivial, as several drawbacks such as shading, depth-resolution, limited field of views, spheroids going out of focus, hydrogel swelling, distinguishing spheroids from entrapper air bubbles and other artifacts, limited data acquisition, and subsequent analysis [26, 31, 32]. Conventional methods based on traditional microscope analysis cannot overcome these drawbacks, and the resulting images are often blurred and misplaced, thereby impairing morphological analysis. Nevertheless, there is a need for the development of 3D imaging methods that enable automated and quantitative analysis of spheroids embedded in hydrogel systems [31]. More recently, some interesting automated imaging pipelines have been reported for analyzing spheroids, but they have focused solely on high-throughput platforms [33–35]. Some of them employed hydrogels, but their setups were limited to predefined spatial conformations [33] or to tiny surface areas [35], which were not suitable for analyzing multiple spheroid interactions. Therefore, the objective of this work was to develop a robust and automated pipeline for accurately tracking and measuring spheroids encapsulated in hydrogels across larger areas, without spatial constraints, ideal for scaling up tissue engineering, as well as for other advanced applications such as drug screening platforms, embryogenesis, and spheroid dynamic studies.

Here, we focus on the migration behavior of hMSC spheroids in a hydrogel without cell adhesive motifs, an area that remains understudied, for which an automated pipeline for tracking and measuring has not yet been established. This is a need for the tissue engineering field since hydrogels without cell adhesive motifs generally have a low-viscosity character (except hydrogel gums) and are usually employed with hydrogels with cell adhesive motifs to increase the overall hydrogel viscosity and enable the manufacturing of 3D models, scaffolds and bioprinted constructs [36]. Since XG, Alg, and HAMA are good examples of widely explored polysaccharide-based hydrogels without cell-adhesive moieties, they were the focus of this study. Additionally, they employ different crosslinking strategies; XG–Alg blend is ionically crosslinked with calcium ions [13], whereas HAMA is covalently crosslinked in the presence of light [15]. Furthermore, XG is a branched and high-molecular-weight polysaccharide, whereas Alg and HAMA have linear networks with medium-to-low molecular weights. Using this automated pipeline, we first compared the dynamic interactions caused by the swelling effect of XG–Alg compared to HAMA (ionic versus photo-crosslinking mechanisms). Then, we assessed morphological changes of hMSCs spheroids into XG–Alg, including reversible spheroid-ellipsoid shapes, axis rotational motion, outermost layer movements, spheroid fusion, and spheroid migration speed. Finally, we evaluated the overall dynamics of spheroid-protruded cluster , tracking these with automated calculations of several parameters, including maximum distance, path length, cell cluster migration speed, and direction. A schematic illustration of our automated pipeline is shown in figure 1.

2. Materials and methods

2.1. Culture conditions and production of hMSC spheroids

Human mesenchymal stromal cells (hMSCs, 8F3543, Lonza) were expanded by culturing 3000 cells cm^{-2} up to 70% of confluence (passage 7), at 37 °C under a 5% CO_2 atmosphere. For all experiments, alpha MEM culture medium with GlutaMAX (32561-029, Gibco) was used, supplemented with 10% (v/v) fetal bovine serum (FBS, F7524, Sigma-Aldrich) and 1% penicillin/streptomycin solution (11548876, Thermo Fisher). A microwell array insert was employed to produce hMSC spheroids, as previously described [37]. Briefly, 5×10^5 cells were seeded into each microwell array to obtain 164 spheroids containing an average of 3048 cells per spheroid. The cells in the microwells were then cultured for 5 days (d) to form highly spherical and compact spheroids. The culture medium was refreshed every 48 h.

2.2. Encapsulation of hMSC spheroids in the XG–Alg hydrogel

A polysaccharide hydrogel composed of a mixture of xanthan gum (XG) and alginate (Alg) was employed to encapsulate hMSC spheroids. The hydrogel, with a final concentration of 3.75% XG and 1.12% Alg (w/v) in PBS (XG–Alg), was freshly prepared and sterilized for each experiment, as previously described by Decarli *et al* [13]. To prepare the samples for the live cell experiments, 100 μl of XG–Alg hydrogel was placed in a 96 flat-bottom well plate ($N = 10$ wells) and centrifuged (2000 g, 5 min) to obtain a thin hydrogel layer as free of bubbles as possible. HMSC spheroids were collected from the microwell array inserts, washed twice with PBS, and randomly mixed into this thin hydrogel layer. Ionic crosslinking was performed using $CaCl_2$ (200 μl, 125 mm) for 10 min. Samples were washed with PBS twice and covered with the culture medium. When brightfield microscopy monitoring was not able to provide enough segmentation power, hMSC were

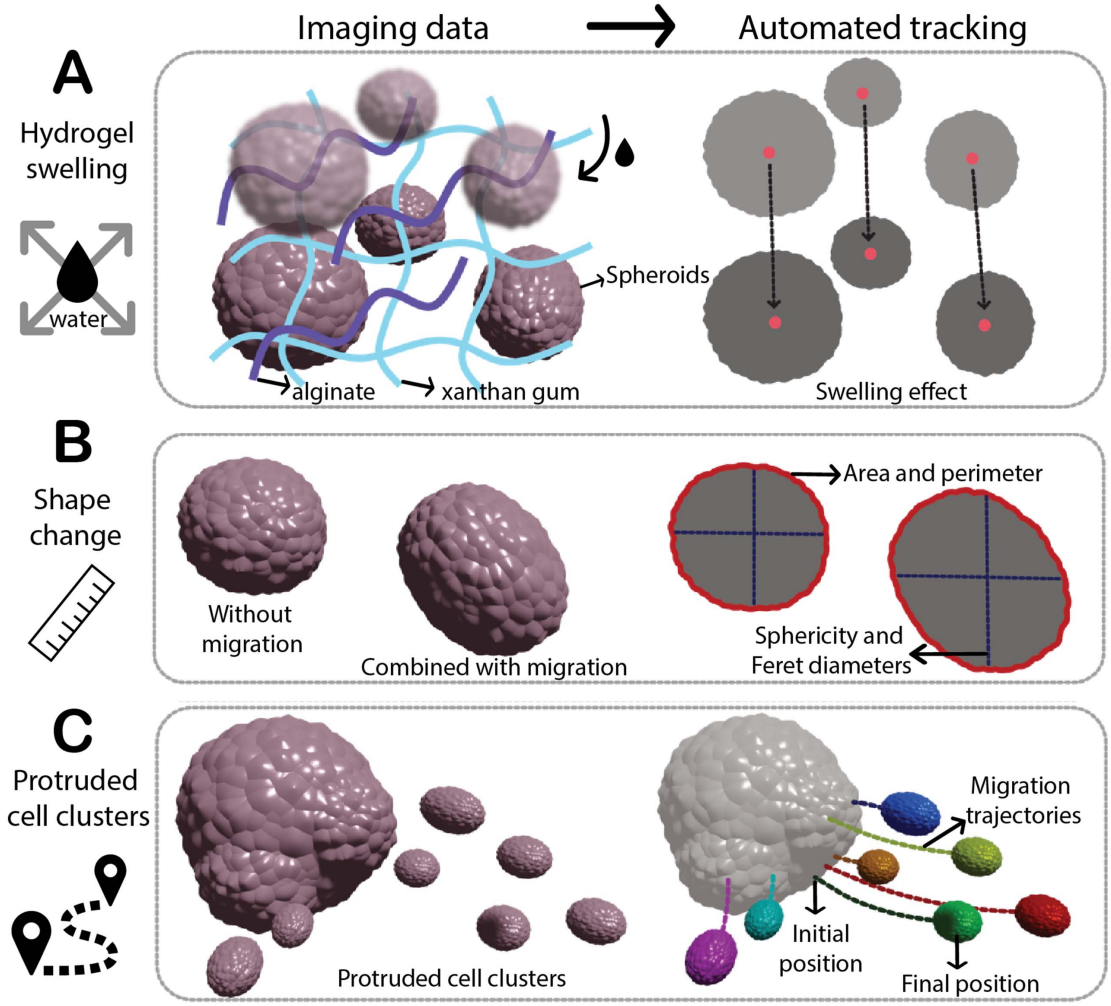

Figure 1. Automated pipeline developed for tracking and measuring spheroids in complex 3D hydrogel systems. (A) Dynamic interaction between the xanthan gum-alginate hydrogel and hMSCs spheroids due to the swelling effect. (B) Shape changes in the absence or combined with spheroid migration. (C) Cell protrusions and migration of protruded cell clusters from the spheroids within the hydrogel.

stained using 1 μm CellTracker^{TM} deep red dye after 1 mm DMSO reconstitution following manufacturer instructions (C34565, Thermo Fischer) and Hoechst 33342 nucleic acid stain in a 1 μg ml^{-1} concentration (H1399, Thermo Fischer). Spheroids were collected from the microwell and incubated with both dyes in a 15 mL tube, in the dark and at 37 °C for a maximum incubation period of 10 min. To avoid spheroid clumping and ensure efficient staining penetration, a gentle tap was performed every 2 min to maintain spheroids in suspension. Spheroids were washed twice in PBS before being mixed into a thin layer of XG–Alg hydrogel.

2.3. Encapsulation of fluorescent beads in XG–Alg and HAMA hydrogels

Fluorescent polystyrene beads with a mean diameter of 160 μm (35–14, Thermo Fisher Scientific) were used in control experiments to mimic hMSC spheroids. The samples were prepared using the same protocol described in section 2.2, but encapsulating the fluorescent beads instead of hMSC spheroids in a thin layer of XG–Alg or HAMA hydrogel. The HAMA hydrogel was synthesized following the protocol described by Sanchez *et al* [15], with no modifications. Briefly, a 2% (w/v) solution of 200 kDa sodium hyaluronate (HA, Lifecore Biomedical) was prepared in deionized water, and the pH was adjusted to 8.5 using a 1.0 m sodium hydroxide solution. Methacrylic anhydride (Sigma-Aldrich) was added dropwise under continuous stirring while maintaining the pH between 7.5 and 8.5. The reaction proceeded on ice for 2 h before being stopped with excess deionized water. The product was purified via dialysis against deionized water for seven days, followed by lyophilization. The final degree of functionalization of 46% was quantified using 1 H NMR spectroscopy. HAMA hydrogels were prepared at a concentration of 2% (w/v) in PBS. Fluorescent beads were homogeneously dispersed in the HAMA solution using the same protocol described in section 2.2 and crosslinked via photopolymerization using 0.1% (w/v) lithium

phenyl-2,4,6-trimethylbenzoylphosphinate (LAP, Sigma-Aldrich), under UV light exposure (365 nm, with an intensity of 12 mW cm^{-2} for 30 s).

2.4. Live-cell imaging experiments

Time-lapse microscopy was performed using a Nikon Eclipse TI-E microscope (Japan) with an Okolabs environmental control system (37 °C and 5% CO_2 atmosphere) equipped with a Prime 95B sCMOS camera and Lumencor Spectra X Light source. The time-lapse imaging package of NIS Elements Software (Nikon, Japan) was used to monitor the experiments, together with a motorized high-accuracy image capture system. The analysis was based on spheroid and cell cluster motility. To overcome small disturbances, the well plate was maintained in static and dark conditions inside the microscopy incubator between image acquisition and no media change or any other type of movement was performed. For the longest experiments, the total well volume was filled with media to ensure nutrient supply (approximately 1:3 hydrogel/media ratio). To ensure control of the atmosphere humidity, the remaining empty wells of the 96-well plate were filled with PBS to aid during the time-lapse data acquisition experiment.

2.5. Swelling ratio

The swelling ratio of the XG–Alg hydrogel, as well as two additional hydrogel controls made of their single components (solely $XG_{3.75}$ and $A_{1.12}$), was determined after exposure to either PBS or culture medium at 37 °C. The samples were carefully prepared as described in 2.2 (not encapsulating spheroids), and their masses were assessed using a high-precision scale (initial mass). Samples were maintained in a cell incubator, and after 2, 4, 6, and 24 h, the excess liquid was removed by blotting, and their masses were immediately determined (final mass). The swelling ratio was calculated as previously described [13].

2.6. Automated pipeline for tracking and measuring spheroids in 3D hydrogel systems

The created pipeline is discussed in detail in section 3.1, as it explains the need for each function employed, which was based on the results obtained in a feed-forward approach. First, 3D-acquired images were transformed into a pseudo-2D image of each *Z*-stack to better delineate and detect spheroid and protruded cell clusters. Then, our pipeline was created based on a sequence of multiple filters/functions for enhancing spheroid borders, creating a *Z*-projection using extended depth of focus, reducing hydrogel shading, and identifying *X* and *Y* coordinates in an automated manner. For the shape change analysis, the filter functions employed in our image pipeline were *extended depth of focus, shading correction, Gaussian Laplace, Region of interest* (ROI), and *filtering*. For the analysis of cellular protrusions from spheroids and migration of protruded cell clusters within the hydrogel, the *parent-child function* was used, in which we tracked the distance between the centroid of individual protruded cells to the closest edge of the spheroid using the *child-distance* function and extracted the distance of the spheroid. Furthermore, the total path covered by the cells and the direction of the cell clusters were analyzed. These multiple filter functions were synergistically integrated into a unique automated pipeline within the NIS-Elements General Analysis (GA3, Nikon) for detecting spheroids and protruding cell clusters over 70 h time-lapse microscopy (figure 2). All data related to tracking and measurements were automatically generated, exported to excel, and a complete set of parameters was calculated. For spheroids, area, sphericity, perimeter, maximum and minimum Feret diameter, and circularity were determined. Migration parameters were simultaneously assessed for both spheroid and multiple protruded cell clusters to automatically obtain migration directions, pattern of trajectories, straightness, the total path length, the maximum distance achieved from the spheroid, and migration speed.

2.7. Statistical analysis

Statistical analysis was conducted using Prism software (10.6 version, GraphPad). Data are shown as mean ± standard deviation (STDEV) or represented using STDEV bars in the graphs. Non-parametric t-test, two-tailed with $p < 0.0.5$ was employed to evaluate statistical significance (ns, non-significant and * significant difference). This study is based on observation, tracking, and measuring spheroids in 3D complex hydrogel systems. Hence, only phenomena observed in at least three replicates were reported, except for the migration of protruded cell clusters that were assessed in duplicate.

3. Results

3.1. Development of an automated microscopy method for time-lapse image acquisition

An automated imaging acquisition method was developed to acquire time-lapse image datasets with both brightfield and fluorescence microscopy. During the implementation of this image acquisition method, we encountered challenges in obtaining automated imaging of spheroids encapsulated in 3D hydrogels, which were attributed to the volumetric assessment inherent to 3D samples and related to the swelling behavior of the hydrogels. Several strategies were developed to guarantee efficient analysis for time-lapse images.

-Imaging considerations to account for the 3D environment and respective strategies to guarantee efficient analysis for time-lapse images

One of the critical settings for image acquisition was to establish the appropriate *Z*-focus, which is not

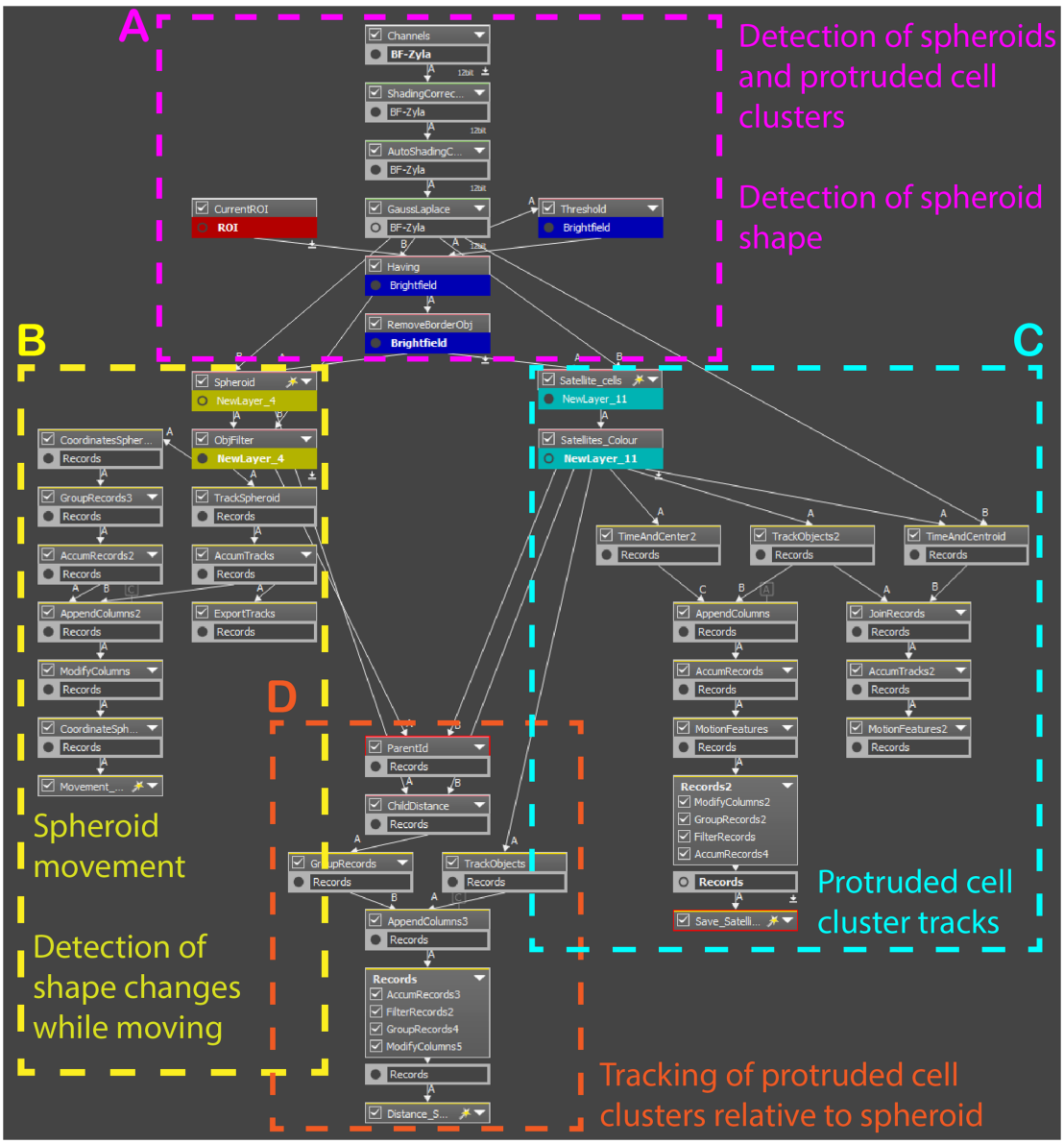

Figure 2. Synergistic integration of a unique automated pipeline for tracking and measuring cell spheroids encapsulated in 3D hydrogel systems. (A) Detection of spheroids, including shape change when in static conditions, and protruded cell clusters (pink path). (B) Tracking spheroid movement, including shape changes while moving (yellow path). (C) Protrusion direction within the hydrogel (green path). (D) The combination of both spheroid and protrusion directions (orange path).

trivial in a 3D hydrogel system. The *Z*-range should encompass the full thickness of the hydrogel, resulting in a higher number of *Z* stacks acquired, which in turn increases the acquisition time and leads to larger file sizes. For example, tracking five samples using brightfield and two fluorescence wavelengths with 25 *Z*-stacks for 70 h resulted in a file of around 285 GB. Hence, data analysis and appropriate computational power had to be taken into account, as this would result in lengthy computational analysis while implementing automated tracking and subsequent quantifications. Assuming the imaging setup had the required *Z*-working distance, the analysis can be addressed by utilizing microscopes that offer higher and ideally single-cell resolution. In conjunction, smart microscopy approaches that employ advanced programming and artificial intelligence to perform live tasks during acquisition and improve the datasets prior to analysis. Yet, establishing such a setup can also be a hurdle by itself. To ensure efficient analysis of time-lapse images using a simple strategy, we first divided large files into independent samples. This was followed by the implementation of a focused *z*-project (*Extended Depth of Focus*) to convert a 3D environment into a 2D representation of the stack. This helped to detect and delineate boundaries efficiently, while enhancing automated tracking and subsequent quantifications.

During spheroid movements, the border of the spheroid was often compromised, causing limitations for automated morphological assessment. Furthermore, in the slices within the *Z*-focus depth

that were far away from the *Z*-average region, the automated tracking system easily misidentified entrapped air bubbles as cell spheroids (supplementary figure 1, blue squares). To tackle this, two strategies were investigated. First, to distinguish spheroids from bubbles without causing any external disturbance in the experiment, we extended the recording experiments to longer periods, allowing air bubbles to displace or to gradually exchange with the medium. We further excluded these initial frames from the final analysis. Alternatively, we performed previous staining of spheroids using Hoechst 33342 nucleic acid stain (supplementary figure 2(A)) or in combination with the CellTracker™ Deep Red (supplementary figure 2(B)). Results showed that when using 1 μm CellTracker, the stained spheroids remained viable, allowing improved identification of the outer layer even when multiple spheroids were in physical contact (supplementary figure 2(A)), making this approach ideal for automated morphological assessment for up to 50 h. After that, we identified that the dye signal was reduced and was also gradually eliminated by the cells, remaining within the hydrogel, which compromised the automated assessment due to increased background interference (supplementary figure 3). Higher concentrations of the dyes were tested, aiming to improve the retention within the cells for longer than 50 h. Despite this, no visual improvement was observed until the identification of a threshold dose (10× concentrated dye solution) that resulted in spheroid death, which was also confirmed by the absence of metabolic activity (supplementary figure 4).

-Imaging consideration to account for hydrogel swelling and respective strategies to guarantee efficient analysis for time-lapse images

Due to the typical swelling behavior of hydrogels, we initially assessed the dynamicity of XG–Alg. Initial results indicated that spheroids moved within the hydrogel, and an appropriate *XYZ* focus was not always possible without compromising the upstream morphological analysis of later time-lapse stages. As indicated in supplementary figure 5(A), when the automated imaging monitoring started, four spheroids could be observed at the edge of the settled focused region (pink square). Over time, three of them moved to an area outside the *XY* focus, which impaired tracking analysis, and only one remained. (supplementary figure 5(B)). This was a repeated imaging challenge due to the limited *XY* area selected for imaging. Our results indicated that when the spheroids were centered in the focused region when acquisition started (0 h) (supplementary figure 5(A) and (B), red arrow), the time-lapse tracking was usually successful. For post-processing, to guarantee accurate analysis, we employed a ROI on the image. This strategy helped in focusing on central regions, resulting in higher accuracy of data analysis for longer periods.

Excessive shading was another aspect of imaging that should be considered when imaging these 3D hydrogels. Our results indicated that shading differences were caused by entrapped air bubbles (supplementary figure 6, red arrows), artifacts (supplementary figure 6, yellow arrows), water evaporation, and the presence of heterogeneous hydrogel microregions. The latter reason is commonly observed when employing hydrogel blends, such as the XG–Alg. The excessive shading had a more pronounced effect on the tracking of small, protruded cell clusters that migrated from the main spheroid within the hydrogel (supplementary figure 6, blue square). To address excessive shading, attempts to improve the imaging setup (e.g., increasing light exposure) or sample preparation (extensive hydrogel centrifugation) were insufficient. However, an efficient analysis by our pipeline successfully overcame shading as a post-processing approach. This was based on subsequent steps of functions *shading correction* and a *Gaussian Laplace*, in addition to the inclusion of spheroids and protruded cell clusters within the ROI (figure 2(A)). Hence, we successfully excluded areas with excessive shading, which had caused false positive detection of cell clusters. Lastly, additional analysis of time-lapse images included the function *filtering* applied on different object sizes to distinguish spheroids from small cell clusters, as well as enhancing the *contrast* between the spheroid and cells on one hand, and the hydrogel itself on the other (figures 2(A) and (C)). By succeeding within this function, we could partially mitigate our initial lack of detection, and clean backgrounds were obtained, which highlighted the movements of spheroids and cell clusters before further image quantification (figures 2(B) and (D)). Moreover, we were able to segregate spheroids from cell clusters, allowing us to study the dynamics of the spheroids and the protruding cells independently from the same dataset.

Therefore, by having a complete automated pipeline to mitigate the hydrogel background and enable accurate quantification, we investigated three different phenomena. First, the dynamicity and swelling properties of XG–Alg and HAMA hydrogels, followed by several hMSC spheroid shape changes, and migration trajectories of protruded hMSC cell clusters from the spheroids into the hydrogel. Taking these three aspects into consideration allowed a deeper understanding of spheroid cellular behavior within dynamic hydrogel systems.

3.2. Spheroids versus hydrogel: investigating dynamicity and swelling properties

To first analyze the influence of the properties of the hydrogel matrix on both spheroid, cell motility and imaging, we assessed the dynamicity and

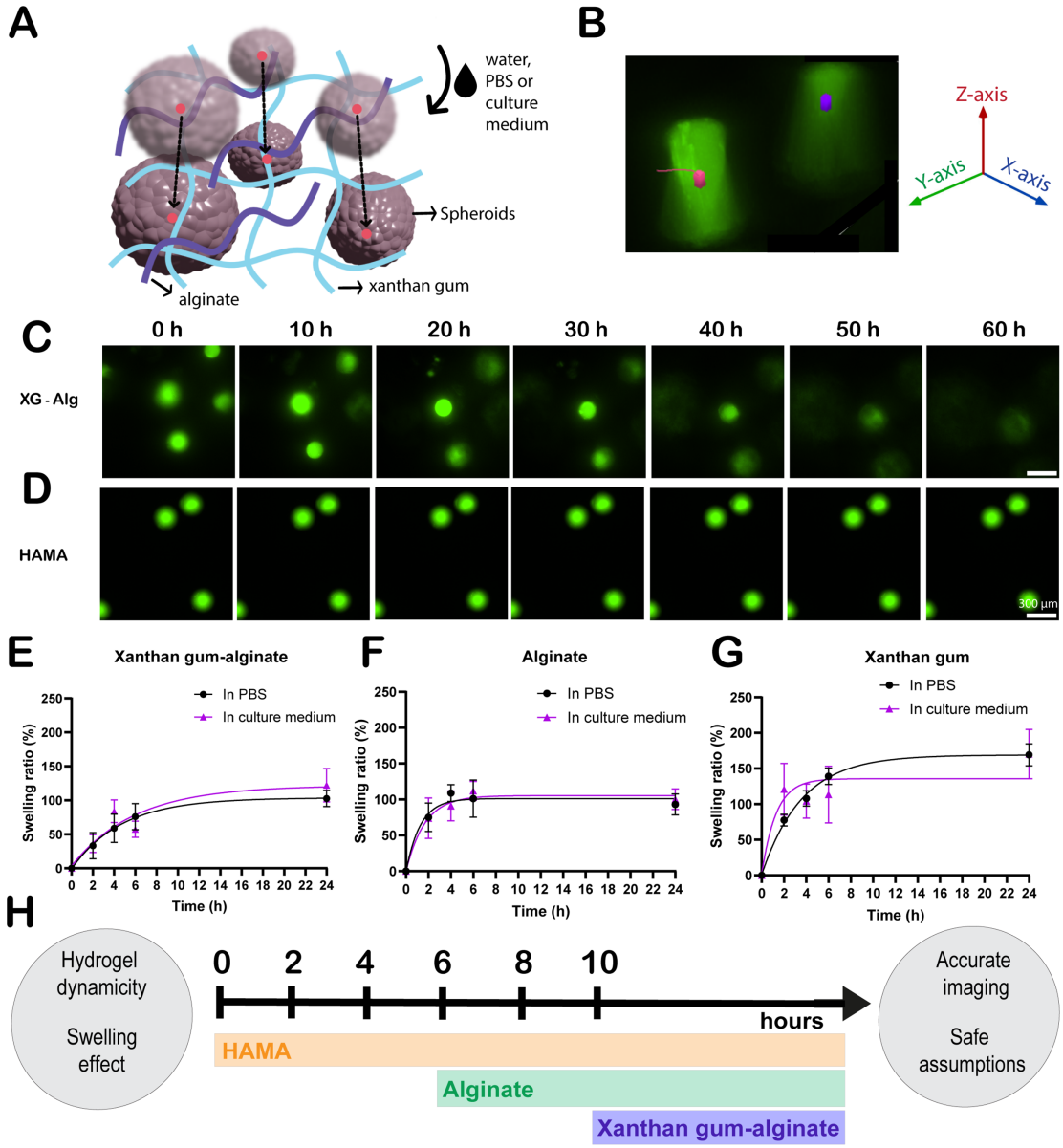

Figure 3. Automated tracking strategy to evaluate the dynamicity of the XG–Alg and HAMA hydrogel networks while encapsulating fluorescent beads. (A) Schematic illustration of the automated pipeline developed for assessing dynamicity and swelling, and (B) a real image during tracking assessment showing the movements of the fluorescent beads in a 3D view due to the dynamicity and swelling of the XG–Alg hydrogel in culture medium. Fluorescent particles tracked in (C) XG–Alg and (D) HAMA hydrogel networks for 60 h (scale bar = 300 µm). (E) Swelling ratio assessed in culture medium and in a chemically defined solution (PBS) for 24 h of the E) XG–Alg hydrogel, (F) alginate (Alg) and (G) xanthan gum (XG), independently. (H) Timeline proposed to jointly consider the dynamicity and equilibrium of different hydrogel systems, e.g. HAMA, alginate, and XG–alginate blends.

swelling behavior of the XG–Alg hydrogel system. As previously reported, this hydrogel was characterized in terms of rheological assessments, stability, mass change, and swelling over 28 d [13]. Although it is a highly viscous hydrogel due to the intrinsic character of natural XG, it can also be considered a soft system, with a stiffness of 1 kPa [13]. Since XG is an efficient thickening agent that tends to absorb enormous amounts of water [36], we aimed to investigate whether the polymeric mesh of XG–Alg hydrogel exhibits high dynamicity that could influence automated imaging, even when crosslinked with calcium ions.

Aiming to assess the dynamicity of the hydrogel, excluding the cell spheroid intrinsic dynamicity, fluorescent beads with a diameter equivalent to the hMSC spheroids were encapsulated in the XG–Alg hydrogel, and the movements of beads were assessed up to 60 h exposed to culture medium, as schematically depicted in figures 3(A) and (B). After analyzing the tracking images of the XG–Alg hydrogel, we observed a displacement of the beads in the matrix during the first 10 h, which indicated that this high dynamicity could be correlated with a rapid swelling of XG–Alg (supplementary video 1). However, the swelling may have become less

pronounced somewhere between 0 and 10 h in culture, when the beads appear to have achieved their equilibrium, from 10 to 40 h (figure 3(C)). After 40 h, the fluorescent beads began to settle towards the bottom hydrogel layer and moved out of the set Z-plane at 60 h.

For comparison purposes, HAMA with the same stiffness as XG–Alg (1 kPa) was used as a comparison. In contrast to what was observed for XG–Alg, the beads encapsulated in the HAMA hydrogel were completely static throughout the whole experiment, from 0 to 60 h, indicating that this hydrogel formulation did not swell significantly (figure 3(D)). Besides the similarities of these hydrogel systems in terms of mechanical properties, XG–Alg was ionically crosslinked with calcium ions, while HAMA photocrosslinked via methacrylate groups (covalent crosslinking).

To corroborate the microcopy observations, we assessed the swelling ratio of the hydrogels, taking into consideration the conditions used in the automated analysis. The results showed significant swelling of XG–Alg in the culture medium until 6 h, reaching an increase of 75% in the swelling ratio at this timepoint (figure 3(E)). Additionally, employing a nonlinear fitting curve analysis (considering a 24 h period), resulted in the equilibrium being experimentally reached at around 10–12 h, which continued for up to 24 h. These results corroborate our automated spheroid tracking analysis, in which high dynamicity of the hydrogel occurred in the first 10 h of imaging. Since we used culture media supplemented with fetal bovine serum to replicate the conditions used when culturing hMSC spheroids and the bead experiment, an additional experiment with PBS was performed to analyze the behavior of the hydrogel using a chemically defined solvent. As a result, the same trend was observed (figure 3(E)). Hence, the experimentally assessed swelling effect validated the dynamic phenomena observed by the automated imaging, even when using two different solvents. Considering the swelling observed in the first 10 h, when imaging a blend of XG–Alg, caution should be taken in the inclusion and analysis of these early timepoints, as they can drastically impact the material and cellular dynamics interpretations. For shape change analysis (section 3.2) and migration of protruded cells (section 3.3), we excluded the initial 10 h to exclude the pronounced effect of the hydrogel swelling effect, focusing as much as possible on cell-driven movements of spheroids and cell clusters.

Due to the extensive dynamicity observed in the blend of XG–Alg, we investigated the polysaccharides individually to identify the primary responsible for such a high swelling ratio. The result showed that Alg undergoes considerable swelling (an increase of 75% on average) in the first 2 h, but stabilizes after reaching a plateau of approximately 100% after 4 h. From 4 h until 24 h, the swelling ratio remains unchanged in both PBS and culture medium (figure 3(F)). XG hydrogel, on the other hand, swelled 78 $\pm$ 8% in the first 2 h and 169 $\pm$ 15%, after 24 h in PBS. In the presence of culture medium, the swelling ratio reached 120% on average in the first 2 h. In earlier timepoints, variable results were obtained, which may be attributed to protein attachment to XG from culture media supplemented with FBS, as reported before [13]. Thus, a significantly higher swelling ratio was observed for XG matrix alone, without an evident equilibrium within the 24 h investigated (figure 3(G)). Interestingly, this intense swelling ratio could be considerably reduced and controlled when XG was blended with alginate (figure 3(E)), probably due to the strong crosslinking effect of calcium ions with alginate combined with the non-covalent chemical interaction between the two polymers.

Taking these results into consideration, the swelling behavior of the hydrogels used for encapsulating spheroids should be considered for the data analysis and interpretation. Ideally, hydrogels should be stable to uncouple the cell dynamics as much as possible from the hydrogel swelling. Our results indicated that the timeline for starting the analysis depends on the hydrogel formulation, where image acquisition could begin at 0 h for HAMA, after 6 h for Alg, and after 10 h for XG–Alg (figure 3(H)). Excluding these early timepoints, where hydrogel swelling is predominant, could be used to simplify data acquisition and subsequent analysis. Despite this, it is important to consider that these early-stage events might be determinants of the overall system dynamicity.

3.3. Shape changes of hMSC spheroids embedded into XG–Alg hydrogel

The pipeline enabled us to extract automatically the spheroid coordinates and diverse morphological data for accurate quantification, including area, perimeter, minimum and maximum Feret length, and circularity (used to calculate sphericity). Several morphological changes were noticed in spheroids during migration (figures 4(A)–(C)) and also in the absence of noticeable migration (figures 4(D)–(F)) in the XG–Alg hydrogel. In several cases, spheroids could easily undergo major structural deformation, assuming an ellipsoid form [5], a symmetric oval-shaped structure less investigated than the spheroid. During migration, spheroids also showed reversible conformation changes, from ellipsoid to spheroid within a period of 23 h (figures 4(A) and (B)), with a new change to elliptical conformation within 46 h (figure 4(C)). These shape changes observed in spheroids were frequently associated with migration, resulting in a measured average migration speed of 1.2 μm h^{-1}, detected for hMSC spheroids with a mean diameter equal to 178.3 $\pm$ 4.0 μm embedded into the XG–Alg hydrogel.

Spheroids were also able to rearrange their conformation to perform rotational motion around their

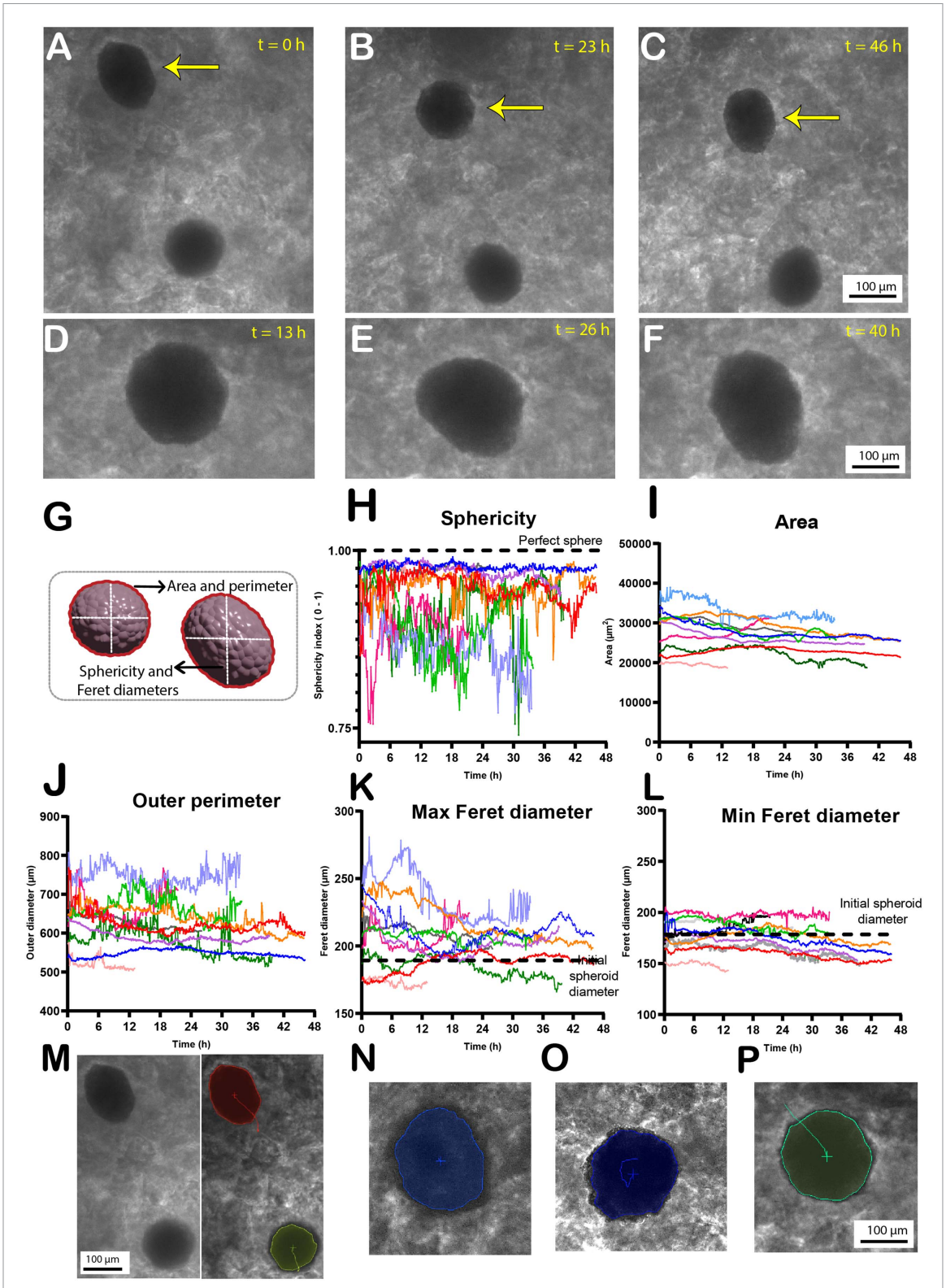

Figure 4. Automated tracking and measurements of shape change of hMSC spheroids encapsulated into the crosslinked XG–Alg hydrogel. (A)–(C) During a combined migration movement, a representative case of a reversible conformation change (ellipsoid to spheroid and back to ellipsoid) during 46 h of measurement. (D)–(F) Representative case of a spheroid turning into an ellipsoid after 40 h in the absence of noticeable migration. (G) Schematic illustration of the automated pipeline developed for shape change tracking and quantification. (H)–(L) Several morphological parameters were simultaneously assessed, and data were automatically generated regarding (H) sphericity, (I) area, (J) outer perimeter, (K) maximum Feret diameter, (L) min Feret diameter. (M) Tracking the migration trajectories of spheroids. Through identification of the centroid, a line that follows the centroid trajectory is drawn simultaneously with tracking shape change deformations, allowing the identification of (N) absence of migration, (O) circular trajectories around their axes, and (P) larger migration trajectories.

axis. An intense movement of the cells present in the outermost layers of spheroids was observed, demonstrated by a flexible and less dense cells-ECM network, which facilitated cell motility (supplementary videos 2–4). On the other hand, a darker, compact, and more dense area is noticed in the core of these spheroids (supplementary figure 7). This indicates that a denser cell-ECM network was concentrated in the core, where the cells were unable to move freely, in contrast to the outermost layers, where cells acted as motile cilia, with the capability to coordinate movement to propel the entire 3D spheroid. Finally, shape change was also noticed during spheroid fusion processes (supplementary video 5).

To study these types of movements, manual tracking and measurements are possible, although extremely laborious and inefficient, especially considering long time-lapses. The automated pipeline allowed for monitoring and simultaneously assessing and measuring shape change (figure 4(G)). This was measured through several morphological parameters of hMSC spheroids encapsulated in the XG–Alg hydrogel (figures 4(H)–(L)). The sphericity (figure 4(H)) varied from 0.75 to 0.98, thus indicating a dynamic remodeling from a loose to tight conformation for most spheroids over 46 h. Sphericity is relevant for determining the uniformity of spheroids, where values higher than 0.95 indicate an almost perfectly shaped sphere (example of one spheroid, blue line in the graph). The spheroid area (figure 4(I)) was maintained at a slightly constant level over the whole experiment duration, whereas the outer perimeter oscillated significantly (figure 4(J)). This confirms that the outermost surface layer of spheroids was more active in terms of movements than the core, corroborating the previous observations (supplementary video 2–4). The Feret diameter (figures 4(K)–(L)) allowed for monitoring the elongation from spheroids to ellipsoids through the analysis of the caliper lengths (min and max). The Max Ferret is the longest distance between any two points along the selection boundary, and the Min Ferret is positioned at 90° to the first, while also measuring the longest distance between the selection boundary. HMSC spheroids oscillated significantly in the Max Feret (figure 4(K)) and much less in the Min Feret (figure 4(L)), demonstrating an intense reversible spheroid-ellipsoid change.

Finally, the developed automated pipeline was also useful for tracking the migration trajectories of spheroids. Through the identification of the centroid, we tracked the movement of the centroid during spheroid migration, while simultaneously tracking shape change deformations (figure 4(M) and supplementary video 6). Using this tool, it was possible to identify the absence of migration (figure 4(N)), the noticeable circular trajectories around spheroid axes (figure 4(O)), and larger migration trajectories (figure 4(P)).

3.4. Cellular protrusions from spheroids and migration of protruded cell clusters

Upon the analysis of the spheroid shape changes and movement as previously described, we also observed the movement of the cell clusters, which was analyzed independently, using an additional module on the developed pipeline (figure 2(D)). With this approach, the distance from the protruded cells to the spheroid was determined over time. This allowed us to monitor and quantify the diverse peripheral movements of cell clusters observed around the spheroids. As a result, diverse migration parameters were simultaneously assessed to automatically obtain migration directions, pattern of trajectories, straightness, total path length, maximum distance achieved from the spheroid, and migration speed.

While analyzing single spheroids, it was possible to observe the formation of cellular protrusions, followed by the detachment of cell clusters from the spheroid surface, which migrate into the hydrogel, as schematically illustrated in figure 5(A), and experimentally observed in figure 5(B). Two different phenomena were identified, one characterized by cell migration without return to the main spheroid (as shown in figure 5(C), blue arrows, and supplementary video 7(A)) and the other characterized by migration of the protruded cells and return to fusion in the main spheroid (as shown in figure 5(D) and supplementary video 7(B)). Supplementary videos 7 A and B clearly show these two contrasting phenomena. These two examples were further analyzed during 70 h with the automated tracking pipeline. Results showed that 83 and 173 cell clusters protruded from the migration samples without and with return, respectively. Furthermore, when investigating the migration direction (figure 5(E)), we identified that protruded cell clusters migrated with a direction varying from 16° to 311° of the spheroid center with minimal differences between the two examples. Thus, they were migrating arbitrarily within the hydrogel, independently of whether they returned to the main spheroid or not. Regarding their trajectories, we identified that they did not migrate in a straight line, but in movements of zig–zag or waves (figure 5(F)) with straightness ranging extensively from 0.025 to 0.943 (figure 5(G)). The average fitting lines of these trajectories, which were related to time and distance from the spheroid, were also determined (supplementary figure 8). This indicates that a hydrogel was heterogeneous and could not guide cell motility, which can be generally attributed to the branched and randomly polymeric network of the XG-A.

Regarding total path lengths, the protruded cell clusters that traveled a maximum path length within the XG–Alg hydrogel achieved a distance of 729 μm (figure 5(H)). However, the maximum distance achieved from the main spheroid (considering a line that passes through the spheroid and the protruded

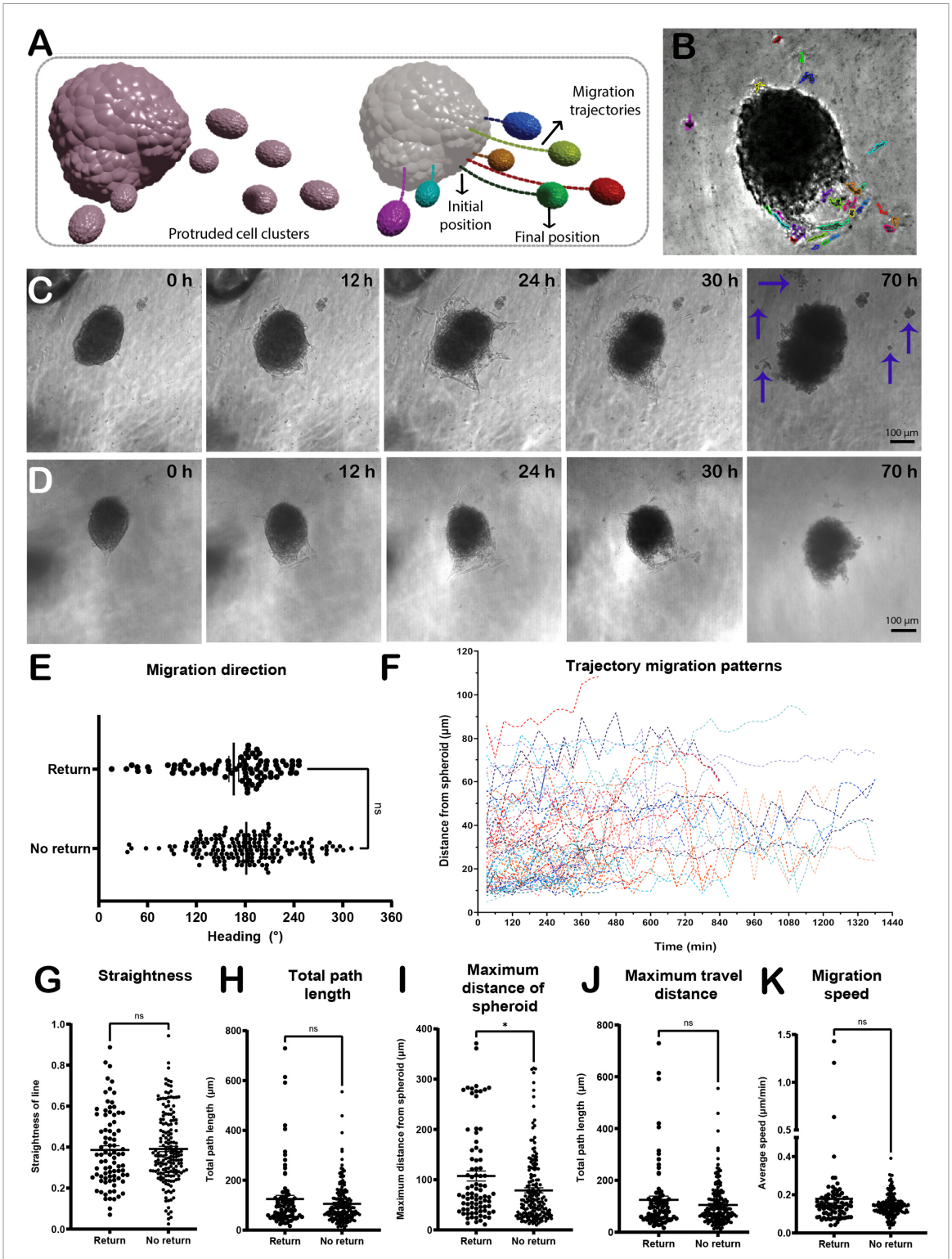

Figure 5. Automated tracking and measurements of protruded cell clusters migrating within the crosslinked XG-A hydrogel. (A) Schematic illustration of the automated pipeline developed for protrusion of cell clusters tracking and quantification and (B) a real image during tracking assessment. Representative cases of the phenomena characterized by (C) cell cluster migration without returning (blue arrows pointing to the cell cluster that remained in their positions at 70 h and (D) with return to the main spheroid after 70 h. Several migration parameters were simultaneously assessed, and the data were automatically generated: (E) migration direction, (F) trajectory migration patterns, (G) straightness, (H) total path length, (I) maximum distance of spheroid (considering a line that passes through the spheroid and the protruded cell cluster), (J) maximum travelled distance (not straight, in zig–zag or waves movements) and (K) migration speed of cell clusters that return and not to the main spheroid.

cell cluster) was always below 400 μm (figure 5(I)). On average, the majority of protruded cells traveled an average distance of 125 μm from the main spheroid, but not in a straight line, but in movements of zig–zag or waves (figure 5(H)). Interestingly, we found that the average total path for cells that did not return was 123 μm (maximum distance from the spheroid), whereas for those that did return,

it was 52 μm (figure 5(J)). Surprisingly, a couple of protruded cell clusters reached a distance of 371 μm from the spheroid and did not return. Regarding speed (figure 5(K)), the average for protruded cell clusters migrating in the XG–Alg hydrogel was 11.4 $\pm$ 12.7 μm h^{-1}, 8.75 times faster than the average speed of spheroids (1.3 μm h^{-1}). Interestingly, when the protruded cell clusters did not return to the main spheroid, some clusters exhibited rapid migration, with speeds reaching 0.4, 0.6, 1.2 and 1.4 μm min^{-1}. Thus, the faster protruding cell clusters we could assess (1.5 μm min^{-1}) reached a migration speed in the hydrogel that was 70 times faster than that of a spheroid. Since spheroids had a diameter of 178.3 $\pm$ 4.0 μm and satellite cells had a much smaller diameter (varying from 10 to 30 μm), the polymeric branched mesh of the blend hydrogel with XG of high molecular weight impaired the movements of spheroids, but not of the protruded cell clusters.

4. Discussion

Imaging a 3D environment is a challenging task, and even more, setting up reliable automated imaging acquisition methods and subsequent data analysis. However, the ability to monitor and assess 3D environments is critically needed. This becomes even more important as research increasingly adopts 3D models rather than traditional 2D counterparts to accelerate the transition to clinical settings [31]. The automated imaging system described here represents a solid technical advance toward automated analysis of spheroids in complex 3D environments such as hydrogels, containing one or more polysaccharides, crosslinked by ions or photopolymerization. Our pipeline specifically enables analysis without requiring spatial confinement of spheroids, as demonstrated previously [33] and upgrades the 3D environment from tiny surface areas (e.g., 10–50 μl scale [35],) to a bulkier environment containing 100–500 μl of hydrogel, which is essential to investigate spheroid–spheroid and spheroid-hydrogel interactions. Furthermore, our pipeline advances by delivering automated imaging while maintaining a fixed-*z*, and being technically capable of handling files with multiple positions. However, there are technical challenges in moving the stage to multiple positions, which depend strongly on the type of hydrogel employed. As demonstrated in figure 3(H), if the hydrogel is very stable (e.g., HAMA), multiple-region analysis is feasible. Conversely, if the hydrogel remains in motion for extended periods (e.g., in a xanthan gum-alginate blend), large fields of view would be needed to compensate for its movement, which is currently not feasible. Hence, in the presented pipeline, our limitations are the inability to handle multiple regions when the hydrogel exhibits high dynamicity and the lack of high-throughput capability. Some tools are being developed in the field that could overcome these limitations and supplement our approach in the near future. Regardless, this automated pipeline has been successfully applied to evaluate shape changes in hMSC spheroids when encapsulated in XG–Alg hydrogel, as well as the cellular protrusions and protruded cell clusters migrating within the hydrogel. Furthermore, our results indicate that this automated pipeline can facilitate the understanding of several cellular dynamic events occurring in hydrogels with high accuracy and low manual interference, which are essential for the upscaling tissue engineering applications and advanced drug screening platforms.

While developing this automated pipeline for tracking and measuring spheroids encapsulated in hydrogels, several considerations were addressed. While software modules can calculate a wide variety of parameters, a key initial challenge was adequate detection of both the spheroids and the protruded cell clusters, while excluding the background caused mainly by extensive shadowing effects and entrapped air bubbles. The use of the *Extended Depth of Focus* module was important to establish a clearer delineation between the hydrogel and cell boundaries. However, shadowing effects and air bubbles could not be completely filtered, requiring the use of ROIs to include regions with cells and exclude regions with shadows. Ideally, this should, where possible, be optimized, as this did require additional review of the images, and hinders more automated acquisition and (online) analysis. Alternatively, implementation of proper fluorescent markers that can stably show both the spheroid and the protruded cell clusters could help in avoiding the shadowing issue and improve automated pipelines. It is, however, important to note that due to the density and size of the spheroid, a fluorescent signal from a cell tracker will always be significantly brighter than those of cell clusters. While this could allow thresholding based on varying fluorescence intensity, we observed that the combination of loss of signal over time and the generally low fluorescence intensity of the cell clusters from the start was not sustained for the full timelapse. Instead, with our pipeline, we have shown that only brightfield datasets successfully overcame the challenges with 3D hydrogels while still providing accurate tracking and quantification throughout the timelapse. Such approaches are critical in the case of full detection and tracking in 3D.

Our automated pipeline proved useful to assess the influence of the dynamicity and swelling of hydrogels on the behavior of the encapsulated hMSC spheroids. In fact, it is becoming widely recognized that the microenvironment and the interstitial matrix surrounding spheroids play a major role in regulating healthy cell cluster or spheroid migration and fusion [28, 38–40]. The XG–Alg hydrogel shows some advantages, such as the stability and transparency for

automated imaging, dynamic rearrangements of its network, allowing the contact and fusion of neighbor spheroids that are closely located [13]. This hydrogel also allows bioprinting structures containing spheroids, that can be successful differentiated towards chondrogenic tissue while offering long-term mechanical support, for up to 56 d [13]. On the other hand, the observed dynamicity during imaging due to the extensive swelling ratio of XG impaired accurate imaging in the first hours of the experiments. Even though this progressive swelling was previously demonstrated [13, 41], herein such swelling could be modulated with the addition of Alg. This blend allowed to achieve a slower swelling kinetics that were more appropriate for automated imaging analysis.

On the other hand, for hydrogels with a low swelling ratio, such as HAMA, our automated pipeline allowed to track fluorescent bead movements throughout the whole experiment. However, this photocrosslinked hydrogel may also not be as adaptable and might not show responsiveness to stimuli, presenting less dynamicity and remodeling potential, which are crucial for the ability to mimic the functionality of human tissues [42]. The main difference between the two hydrogels employed herein lies in their crosslinking strategies. While both had stiffness values of around 1 Kpa, XG–Alg was ionically crosslinked via a reversible electrostatic interaction between carboxylic groups of alginate and calcium. HAMA was photocrosslinked via permanent chemical interaction by covalent bonds to functionalized hyaluronic acid with methacrylate groups [15, 43]. Overall, in our imaging analysis, XG–Alg showed a higher mobility of its network when compared to covalently crosslinked HAMA where no noticeable motility was observed. Indeed, HAMA is often used for achieving spatial patterning while XG and Alg are used as thickeners. Thus, the hydrogel choice is a fundamental point for establishing parameters for automated imaging analysis.

Several shape changes during or in the absence of spheroid migration were observed in this study. While the mechanisms that drive shape changes in spheroids are not yet understood, it is challenging to investigate them by employing *in vitro* experiments. Using a finite element analysis based on molecular diffusion, Leung *et al* [5] proposed that oxygen saturation is the most probable reason for the reversible spheroid-ellipsoid deformation. The authors have shown that when spheroids and ellipsoids show similar volume, the deformed aspect ratio of the ellipsoid enhances its surface area. Modeling oxygen concentration gradients according to this hypothesis has demonstrated that the more elongated the structure (which can be investigated by the Max and Min Feret diameters), the smaller the core-surface distance, and consequently the smaller the oxygen gradients. As a result, the ellipsoids allow more oxygen delivery to the cells regardless of their dimensions [44]. Corroborating with this model, the presence of a hypoxic and necrotic core is often reported in spheroids, unlike in ellipsoids [44]. Hence, the spheroids conformation change observed in the present study might also be related with a response to the concentration of oxygen and nutrients in the microenvironment. Along these lines, shape changes can also be associated with other influences, such as chemotaxis [45] and cellular signaling [21, 23, 46].

When investigating shape changes in cancer spheroids compared to the stem cell spheroids herein studied, another reason could be considered. Cancer spheroids can use conformational changes to improve their motion, resembling an amoeboid, lopopodial or collective cell migration that undergoes constant cycles of protrusion and contraction with significant mechanical distortions in their structures [47, 48]. While for cancer spheroids this may have a potential influence on cancer metastasis, for healthy spheroids with a stem cell character, it might be related to a potential for regeneration or neotissue formation. Further studies are required to validate this hypothesis.

The intense movement in the outermost layers of spheroids, including rotational motion, observed in our study allowed for rearrangements in their conformation and further migration (supplementary videos 2–4), has been reported elsewhere [49, 50]. The authors [49] reported spontaneous rotation in rings of kidney epithelial cells and identified this phenomenon as the natural alignment of cell polarity. Interestingly, they reported that below a threshold perimeter, the cell rings underwent spontaneous rotations, concluding that spontaneous coherent motion results from competitions between cell orientations and active molecular cables at boundaries. Here, we employed cell spheroids of the same size, but further investigation employing larger spheroids may yield more comprehensive insights, since these motions are also known to be crucial for embryo morphogenesis [49]. In a more recent study, [50], this phenomenon of cell tumbling was identified for enhancing stem cell differentiation in hydrogels via nuclear mechanotransduction, which is particularly interesting since we observed the same in our study using hMSC spheroids.

The formation of cellular protrusions, followed by the migration of cell clusters towards the hydrogel, was also assessed by the automated pipeline. Several studies reported this phenomenon in the literature, most of them using cancer cell spheroids as models for cancer invasion [27, 51], or using endothelial cells as a model for vascularization, for which sprouting is a sign of angiogenesis [39, 52, 53]. However, none of the studies reported the use of hMSC spheroids in a hydrogel without cell adhesion moieties.

Several studies have shown that an aligned hydrogel network can guide and modulate cell migration [54–57]. Hence, cells would establish a central axis in

which they form cell protrusions, followed by spreading and cluster migration. This often results in fewer protrusions being generated, although the ones produced present higher efficiency in migration, assessed by both faster speed and increased distance travelled when compared with random 3D hydrogel networks [27]. As suggested by Carey *et al* [27] the efficient migration in aligned hydrogels is because cells detect and respond to local ECM structures. In heterogeneous 3D hydrogels, the alignment is absent, which suggests that the cells need to explore the hydrogel matrix, trying to detect ECM structures where they could bind. This premise helps to elucidate the contrasting behaviors of the detached cell clusters observed in our study. Some cell clusters remained for 34 h in the same position, while others performed reversible movement back towards the main spheroid after around 70 h, in an apparently stochastic manner. The XG–Alg polymeric matrix used herein is made of a heterogeneous network that does not have any type of structural alignment, anchoring moieties, aligned fibers, or micropores. This might explain why cells were moving randomly in the surroundings of the spheroid without a preferred direction.

HMSCs spheroids consist of cells that may exhibit multiple roles, being less dynamic when compared to endothelial cells, for example, which create channels or organized structures typical of angiogenic responses [39]. Stem cells secrete various types of matrix metalloproteinases (MMPs) to remodel the ECM for regulating the ECM-cell interactions and cell fate [58]. However, the expression of MMPs as mediators of physical adaptation and cell motility can be induced by the 3D environment, triggered by diseases, or regulated during tissue development [58]. Thus, stem cell spheroids seem to be less active in terms of migration and sprouting compared to specialized cell types. Indeed, in our study, the average distance of hMSC protruded cell clusters that did not return to the main spheroid was 123 μm, whereas those that did return were an average of 51 μm from the main spheroid. Only 2.5% of the cell clusters could reach a larger distance (371 μm) from the main spheroid within 70 h. When compared with human microvascular endothelial spheroids in a collagen matrix, more intense sprouting was observed, reaching on average, a distance of 230 μm in only 24 h, with some clusters reaching more than 500 μm of distance from the main spheroid [39]. Thus, the absence of cues to guide the cells throughout the hydrogel network, along with the stem cell character of spheroids, may justify the fact that they migrate less and in a random pattern. Hence, the most probable cause for hMSC cell migration within the hydrogel formulation tested remains unclear.

Herein, we developed a pipeline using the NIS software to process images acquired on a Nikon microscope, but in principle, it can be used with images generated in any other microscope that allows further analysis in any software that includes a 3D tool package. The pipeline shown in figure 2 provides useful insights that can be adopted in other imaging software. Moreover, if the proper metadata is available, any TIFF image can be used, relying as well on the performance of the software, as previously addressed elsewhere [59]. For example, our team has successfully tested similar pipelines to quantify data from other microscope brands, as well as data from microCT scans. For this, proper licenses are needed and a translation of the algorithm. Hence, this is a flexible, intuitive, and automated pipeline that has great potential for imaging and tracking within complex 3D cell systems.

5. Conclusion

An automated pipeline was successfully developed to track and measure shape changes of encapsulated spheroids within a 3D hydrogel with a high swelling ratio. This pipeline was also used to quantify protrusion of cell clusters from spheroids and their migration within the hydrogel. This pipeline successfully overcame several constraints for real-time imaging monitoring, namely Z-resolution, shading, hydrogel swelling and dynamicity, and limitations in data and processing. This pipeline proved to be robust enough to enable the simultaneous analysis of both spheroids and hundreds of protruded cell clusters, thereby obtaining a set of shape and migration parameters automatically. Cell cluster migration speed and the maximum distance reached from the spheroid embedded within a hydrogel are crucial parameters for biofabrication of tissues, as well as for emulating diseases such as the spreading of cancer cells. Yet, they are rarely available. Furthermore, this pipeline was easily employed for hydrogels involving one or more polysaccharides and proteins, crosslinked by ions or photopolymerization. This offers an efficient tool to understand the dynamicity of hydrogels and to obtain accurate data that considers hydrogel swelling and mesh movements. Hence, this pipeline brings significant advances to these 3D model systems and other correlated applications.

Acknowledgment

The authors would like to acknowledge the support for this research by the European Union's Horizon 2020 framework program, call SC1-BHC-07-2019—Regenerative medicine: from new insights to new applications, JointPromise—Precision manufacturing of microengineered complex joint implants, under grant agreement 874 837. Project website: www.jointpromise.eu/). Also to the National Council for Scientific and Technological Development (Conselho Nacional de Desenvolvimento Científico e Tecnológico—CNPq, Brazil—Grants # 314 724/2021-4, 307 829/2018-9, 430 860/2018-8, 142

050/2018-0 and 465 656/2014-5), the Coordination for the Improvement of Higher Educational Personnel (Coordenação de Aperfeiçoamento de Pessoal de Nível Superior CAPES, Brazil—Finance codes 001, PrInt 88 887.364849/2019-00 and PrInt 88 887.310405/2018-00), the Fund for Support to Teaching, Research and Extension from the University of Campinas (Fundo de Apoio ao Ensino, à Pesquisa e à Extensão—FAEPEX/UNICAMP, Brazil—Grants # 2921/18, 2324/21) and the NWE INTERREG BONE grant (#495). The authors would like to thank Dr Pinak Samal for the fruitful discussions on the time-lapse microscopy. Finally, the authors would like to preserve and share the scientific legacy of our colleague Dr Jorge Vicente Lopes da Silva, who actively participated in this study and, unfortunately, passed away before it could be published.

Data availability statement

All data that support the findings of this study are included within the article (and any supplementary files). Raw datasets are available at https://doi.org/10.34894/TWQCV9. The microscope time-lapse images can be obtained from the corresponding authors upon request.

Supplementary data available at https://doi.org/10.1088/1758-5090/ae4893/data1.

Supplementary data Video 1 available at https://doi.org/10.1088/1758-5090/ae4893/data2.

Supplementary data Video 2 available at https://doi.org/10.1088/1758-5090/ae4893/data3.

Supplementary data Video 3 available at https://doi.org/10.1088/1758-5090/ae4893/data4.

Supplementary data Video 4 available at https://doi.org/10.1088/1758-5090/ae4893/data5.

Supplementary data Video 5 available at https://doi.org/10.1088/1758-5090/ae4893/data6.

Supplementary data Video 6 available at https://doi.org/10.1088/1758-5090/ae4893/data7.

Supplementary data Video 7 available at https://doi.org/10.1088/1758-5090/ae4893/data8.

Conflict of interest

The authors declare no conflict of interest.

Author contributions

Monize Caiado Decarli 0000-0002-7100-3394
Conceptualization (lead), Data curation (equal), Formal analysis (equal), Investigation (equal), Methodology (equal), Software (equal), Writing – original draft (lead), Writing – review & editing (lead)

Adrián Seijas-Gamardo 0000-0002-8950-367X
Data curation (equal), Formal analysis (equal), Investigation (equal), Methodology (equal), Writing – review & editing (equal)

Timo Rademakers 0000-0003-0286-418X
Methodology (equal), Resources (equal), Software (equal), Validation (equal), Writing – original draft (equal), Writing – review & editing (equal)

Ane Albillos Sanchez 0009-0006-0596-402X
Investigation (supporting), Methodology (supporting), Validation (supporting)

Paul Wieringa 0000-0002-3290-5125
Supervision (equal), Validation (equal), Writing – review & editing (equal)

Jorge Vicente L Silva
Conceptualization (equal), Project administration (equal), Resources (equal), Supervision (equal), Writing – review & editing (equal)

Ângela Maria Moraes 0000-0002-5813-332X
Conceptualization (equal), Project administration (equal), Resources (equal), Supervision (equal), Writing – review & editing (equal)

Lorenzo Moroni 0000-0003-1298-6025
Conceptualization (equal), Project administration (equal), Resources (equal), Supervision (equal), Writing – review & editing (equal)

Carlos Mota 0000-0001-5935-6245
Conceptualization (lead), Funding acquisition (lead), Project administration (lead), Resources (lead), Supervision (lead), Writing – original draft (lead), Writing – review & editing (lead)

References

[1] Laschke M and Menger M 2017 Life is 3D: boosting spheroid function for tissue engineering *Trends Biotechnol.* **35** 133–44

[2] Decarli M C *et al* 2021 Cell spheroids as a versatile research platform: formation mechanisms, high throughput production, characterization and applications *Biofabrication* **13** 1–37

[3] Achilli TM, Meyer J, Morgan JR 2012 Advances in the formation, use and understanding of multicellular spheroids *Expert Opin. Biol. Ther.* **12** 1347–60

[4] Drost J and Clevers H 2018 Organoids in cancer research *Nat. Rev. Cancer* **18** 407–18

[5] Leung B M, Lesher-Perez S C, Matsuoka T, Moraes C and Takayama S 2015 Media additives to promote spheroid circularity and compactness in hanging drop platform *Biomater. Sci.* **3** 336–44

[6] Hajdu Z, Mironov V, Mehesz A N, Norris R A, Markwald R R and Visconti R P 2010 Tissue spheroid fusion-based *in vitro* screening assays for analysis of tissue maturation Zoltan *J. Tissue Eng. Regen. Med.* **4** 659–64

[7] Boland T, Mironov V, Gutowska A, Roth E A and Markwald R R 2003 Cell and organ printing 2: fusion of cell aggregates in three-dimensional gels *Anat. Rec. A* **272** 497–502

[8] De Moor L, Fernandez S, Vercruysse C, Tytgat L, Asadian M, Geyter N, Vlierberghe S, Dubruel P and Declercq H 2020

Hybrid bioprinting of chondrogenically induced human mesenchymal stem cell spheroids *Front. Bioeng. Biotechnol.* **8** 1–20
[9] Mironov V, Visconti R P, Kasyanov V, Forgacs G, Drake C J and Markwald R R 2009 Organ printing: tissue spheroids as building blocks *Biomaterials* **30** 2164–74
[10] Mota C, Camarero-Espinosa S, Baker M B, Wieringa P and Moroni L 2020 Bioprinting: from tissue and organ development to *in vitro* models *Chem. Rev.* **120** 10547–607
[11] Sart S, Tsai A-C, Li Y and Ma T 2014 Three-dimensional aggregates of mesenchymal stem cells: cellular mechanisms, biological properties, and applications *Tissue Eng. B* **20** 365–80
[12] Amaral R, Zimmermann M, Ma A H, Zhang H, Swiech K and Pan C X 2020 A simple three-dimensional *in vitro* culture mimicking the *in vivo*-like cell behavior of bladder patient-derived xenograft models *Cancers* **12** 1–13
[13] Decarli M C *et al* 2023 Bioprinting of stem cell spheroids followed by post-printing chondrogenic differentiation for cartilage tissue engineering *Adv. Healthcare. Mater.* **2203021** 1–17
[14] Dong Q, Su X, Li X, Zhou H, Jian H, Bai S, Yin J and You Q 2023 In vitro construction of lung cancer organoids by 3D bioprinting for drug evaluation *Colloids Surf. A* **666** 131288
[15] Sanchez A A, Teixeira F C, Casademunt P, Beeren I, Moroni L and Mota C 2025 Enhanced osteogenic differentiation in hyaluronic acid methacrylate (HAMA) matrix: a comparative study of hPDC and hBMSC spheroids for bone tissue engineering *Biofabrication* **17** 025013
[16] Bouwmeester M C *et al* 2021 Bioprinting of human liver-derived epithelial organoids for toxicity studies *Macromol. Biosci.* **21** 2100327
[17] Ozbolat I T 2015 Scaffold-based or scaffold-free bioprinting: competing or complementing approaches? *J. Nanotechnol. Eng. Med.* **6** 024701
[18] Asadi N, Alizadeh E, Salehi R, Khalandi B, Davaran S and Akbarzadeh A 2018 Nanocomposite hydrogels for cartilage tissue engineering: a review *Artif. Cells Nanomed. Biotechnol.* **46** 465–71
[19] Amsden B 1998 Solute diffusion in hydrogels. An examination of the retardation effect *Polym. Gels Netw.* **6** 13–43
[20] van Griensven M and Balmayor E R 2024 Extracellular vesicles are key players in mesenchymal stem cells' dual potential to regenerate and modulate the immune system *Adv. Drug Deliv. Rev.* **207** 115203
[21] Joshi B S, de Beer M A, Giepmans B N G and Zuhorn I S 2020 Endocytosis of extracellular vesicles and release of their cargo from endosomes *ACS Nano* **14** 4444–55
[22] Kim S J, Byun H, Lee S, Kim E, Lee G M, Huh S J, Joo J and Shin H 2022 Spatially arranged encapsulation of stem cell spheroids within hydrogels for the regulation of spheroid fusion and cell migration *Acta Biomater.* **142** 60–72
[23] Kim S H, Turnbull J and Guimond S 2011 Extracellular matrix and cell signalling: the dynamic cooperation of integrin, proteoglycan and growth factor receptor *J. Endocrinol.* **209** 139–51
[24] Baraniak P R and McDevitt T C 2010 Stem cell paracrine actions and tissue regeneration *Regen. Med.* **5** 121–43
[25] Lawrence T, Beers W and Gilula N 1978 Transmission of hormonal stimulation by cell-to-cell communication *Nature* **272** 501506–984
[26] Zhong J, Zhao T and Liu M 2022 Fluorescence microscopic visualization of functionalized hydrogels *NPG Asia Mater.* **14**
[27] Carey S P, Goldblatt Z E, Martin K E, Romero B, Williams R M and Reinhart-King C A 2016 Local extracellular matrix alignment directs cellular protrusion dynamics and migration through Rac1 and FAK *Integr. Biol.* **8** 821–35
[28] Ho S S, Keown A T, Addison B and Leach J K 2017 Cell migration and bone formation from mesenchymal stem cell spheroids in alginate hydrogels are regulated by adhesive ligand density *Biomacromolecules* **18** 4331–40
[29] Poldervaart M T, Goversen B, de Ruijter M, Abbadessa A, Melchels F P W, Öner F C, Dhert W J A, Vermonden T and Alblas J 2017 3D bioprinting of methacrylated hyaluronic acid (MeHA) hydrogel with intrinsic osteogenicity *PLoS One* **12** e0177628
[30] Vega J C M, Lee M K, Qin E C, Rich M, Lee K Y, Kim D H, Chung H J, Leckband D E and Kong H 2016 Three dimensional conjugation of recombinant N-cadherin to a hydrogel for in vitro anisotropic neural growth *J. Mater. Chem. B* **4** 6803–11
[31] Appel A A, Anastasio M A, Larson J C and Brey E M 2013 Imaging challenges in biomaterials and tissue engineering *Biomaterials* **34** 6615–30
[32] Dong Y C, Bouché M, Uman S, Burdick J A and Cormode D P 2021 Detecting and monitoring hydrogels with medical imaging *ACS Biomater. Sci. Eng.* **7** 4027–47
[33] Jeon H, Kim G, Carpenter J, Colón Y J and Wang Y 2025 Automated high-content, high-throughput spatial analysis pipeline for drug screening in 3D tumor spheroid inverted colloidal crystal arrays *ACS Appl. Mater. Interfaces* **17** 49210–26
[34] Leary E, Rhee C, Wilks B and Morgan J 2018 Quantitative live-cell confocal imaging of 3D spheroids in a high throughput format *SLAS Technol.* **23** 231–42
[35] Heiss J and Tavana H 2024 Automated analysis of extracellular matrix invasion of cancer cells from tumor spheroids *ACS Meas. Sci. Au* **4** 260–6
[36] Decarli M C *et al* 2025 Xanthan gum–iron system: natural, mechanically tunable, bioactive, and magnetic-responsive hydrogels for biomedical engineering applications *ACS Appl. Mater. Interfaces* **17** 51588–604
[37] Decarli M C, de Castro M V, Nogueira J A, Nagahara M H T, Westin C B, de Oliveira A L R, da Silva J V L, Moroni L, Mota C and Moraes Â M 2022 Development of a device useful to reproducibly produce large quantities of viable and uniform stem cell spheroids with controlled diameters *Biomater. Adv.* **135** 1–14
[38] Paupert J, Sounni N E and Noël A 2011 Lymphangiogenesis in post-natal tissue remodeling: lymphatic endothelial cell connection with its environment *Mol. Asp. Med.* **32** 146–58
[39] Blacher S, Erpicum C, Lenoir B, Paupert J, Moraes G, Ormenese S, Bullinger E and Noel A 2014 Cell invasion in the spheroid sprouting assay: a spatial organisation analysis adaptable to cell behaviour *PLoS One* **9** e97019
[40] Beachley V *et al* 2014 The fusion of tissue spheroids attached to pre-stretched electrospun polyurethane scaffolds *J. Tissue Eng.* **5** 1–11
[41] Andreopoulos A G and Tarantili P A 2001 Xanthan gum as a carrier for controlled release of drugs *J. Biomater. Appl.* **16** 34–46
[42] Hafeez S *et al* 2023 In situ covalent reinforcement of a Benzene-1,3,5-Tricarboxamide supramolecular polymer enables biomimetic, tough, and fibrous hydrogels and bioinks *Adv. Mater.* **35** 1–18
[43] Lou J and Mooney D J 2022 Chemical strategies to engineer hydrogels for cell culture *Nat. Rev. Chem.* **6** 726–44
[44] Gheibi P, Zeng S, Son K J, Vu T, Ma A-H, Dall'Era M A, Yap S A, de Vere White R W, Pan C-X and Revzin A 2017 Microchamber cultures of bladder cancer: a platform for characterizing drug responsiveness and resistance in PDX and primary cancer cells *Sci. Rep.* **7** 1–10
[45] McElwain D L S and Pettet G J 1993 Cell migration in multicell spheroids: swimming against the tide *Bull. Math. Biol.* **55** 655–74
[46] Kosheleva N V *et al* 2020 Cell spheroid fusion: beyond liquid drops model *Sci. Rep.* **10** 1–15
[47] Boot R C, Koenderink G H and Boukany P E 2021 Spheroid mechanics and implications for cell invasion *Adv. Phys. X* **6** 1978316
[48] Pagès D-L *et al* 2022 Cell clusters adopt a collective amoeboid mode of migration in confined nonadhesive environments *Sci. Adv.* **8** eabp8416

[49] Lo Vecchio S, Pertz O, Szopos M, Navoret L and Riveline D 2024 Spontaneous rotations in epithelia as an interplay between cell polarity and boundaries *Nat. Phys.* **20** 322–31
[50] Ayushman M *et al* n.a. Cell tumbling enhances stem cell differentiation in hydrogels via nuclear mechanotransduction *Nat. Mater.* **24** 312–22
[51] Riching K M *et al* 2014 3D collagen alignment limits protrusions to enhance breast cancer cell persistence *Biophys. J.* **107** 2546–58
[52] Hsu H H, Ko P L, Peng C C, Cheng Y J, Wu H M and Tung Y C 2023 Studying sprouting angiogenesis under combination of oxygen gradients and co-culture of fibroblasts using microfluidic cell culture model *Mater. Today Bio* **21** 100703
[53] Elomaa L, Lindner M, Leben R, Niesner R and Weinhart M 2023 In vitro vascularization of hydrogel-based tissue constructs via a combined approach of cell sheet engineering and dynamic perfusion cell culture *Biofabrication* **15** 015004
[54] Fraley S I, Wu P-H, He L, Feng Y, Krisnamurthy R, Longmore G D and Wirtz D 2015 Three-dimensional matrix fiber alignment modulates cell migration and MT1-MMP utility by spatially and temporally directing protrusions *Sci. Rep.* **5** 14580
[55] Aubin H, Nichol J W, Hutson C B, Bae H, Sieminski A L, Cropek D M, Akhyari P and Khademhosseini A 2010 Directed 3D cell alignment and elongation in microengineered hydrogels *Biomaterials* **31** 6941–51
[56] LaBelle S A, Poulson A M, Maas S A, Rauff A, Ateshian G A and Weiss J A 2023 Spatial configurations of 3D extracellular matrix collagen density and anisotropy simultaneously guide angiogenesis *PLoS Comput. Biol.* **19** e1011553
[57] Sayer S, Zandrini T, Markovic M, Van Hoorick J, Van Vlierberghe S, Baudis S, Holnthoner W and Ovsianikov A 2022 Guiding cell migration in 3D with high-resolution photografting *Sci. Rep.* **12** 8626
[58] Page-mccaw A, Ewald A J and Werb Z 2007 Matrix metalloproteinases and the regulation of tissue remodelling *Nat. Rev. Mol. Cell Biol.* **8** 221–33
[59] Wieland F, Schumacher A, Roumans N, van Blitterswijk C, LaPointe V and Rademakers T 2022 Methodological approaches in aggregate formation and microscopic analysis to assess pseudoislet morphology and cellular interactions *Open Res. Eur.* **2** 87